Theory of director fluctuations about a hedgehog defect in a nematic drop

Olaf Stenull,[1] Alexis de la Cotte,[1] Sophie Ettinger,[1] Peter J. Collings,[1,2] A. G. Yodh,[1] and T. C. Lubensky[1]
[1]*Department of Physics and Astronomy, University of Pennsylvania, Philadelphia, Pennsylvania 19104, USA*
[2]*Department of Physics and Astronomy, Swarthmore College, Swarthmore, Pennsylvania 19081, USA*

(Received 18 November 2021; accepted 16 March 2022; published 5 April 2022)

We present calculations of eigenmode energies and wave functions of both azimuthal and polar distortions of the nematic director relative to a radial hedgehog trapped in a spherical drop with a smaller concentric spherical droplet at its core. All surfaces interior to the drop have perpendicular (homeotropic) boundary conditions. We also calculate director correlation functions and their relaxation times. Of particular interest is a critical mode whose energy, with fixed Frank constants, vanishes as the ratio $\mu = R_2/R_1$ increases toward a critical value μ_c, where R_2 is the radius of the drop and R_1 that of the inner droplet, and then becomes negative for $\mu > \mu_c$. Our calculations form a basis for interpreting experimental measurements of director fluctuations relative to a radial hedgehog state in a spherical drop. We compare results with those obtained by previous investigations, which use a calculational approach different from ours, and with our experimental observations.

DOI: 10.1103/PhysRevE.105.044703

I. INTRODUCTION

Topological defects play an important role in self organization and elastic properties of liquid crystals (LCs) [1–8]. Nematic drops, in particular, are appealing systems for study of topological defects in LCs because their spatial patterns can easily be visualized optically. It is well known that a charge $+1$ defect, commonly referred to as a hedgehog, arises in a nematic LC (NLC) confined within a spherical drop with homeotropic (perpendicular) anchoring at the inner surface of the drop's outer boundary. Though this boundary condition ensures that the drop contains a hedgehog defect, it does not determine the director configuration throughout the sphere, particularly near the core. The simplest configuration is the radial one in which the director is everywhere parallel to the radial direction, but other configurations with director twist and bend [5,9–13], with a disclination ring encircling [14–18] or above [19] the spherical origin, or with a core exhibiting biaxial nematic order [20] are possible for spheres with radii considerably larger than any core radius.

The hedgehog configuration is more constrained for the case of interest to us in which a spherical drop of radius R_2 encloses a concentric spherical droplet (which we will refer to simply as the droplet) of radius $R_1 < R_2$ again with homeotropic boundary conditions. Though our primary interest is in $R_2 \gg R_1$, our theory applies to all $R_1 < R_2$. Rüdiger and Stark (RS) [5,13] used this model, which favors a local radial alignment, to determine the limit of stability of the radial hedgehog by calculating the point at which the energy of a critical mode vanishes, thus signaling a transition from the radial to some kind of twisted configuration with increasing $\mu = R_2/R_1$. As indicated above, there are several studies that explore configurational features of spherically trapped hedgehogs but relatively few studies that directly address the nature of director fluctuations within the drop [13,16,21,22]. In this article, we undertake a full analytical analysis of the fluctuations of both the azimuthal and polar components of the Frank director at all positions $\mathbf{r} = (r, \theta, \phi)$ of our model radial hedgehog. Our calculations suggest the existence of what we call a twist-bend hedgehog [23] at μ just greater than a critical value μ_c.

In a companion article, we present the results of an experimental study of director fluctuations about a radial hedgehog in a nematic drop [22]. We used video-rate polarized optical microscopy in conjunction with image analysis to measure the spatiotemporal fluctuations of the director field. Many of our experimental drops, which varied in size, exhibited a slow but giant ($\approx \pi/8$ rad) over-all rotational diffusion of the four-leaf-clover-like transmission pattern under crossed polarizers, accompanied by twist fluctuations of adjacent clover leaves relative to one another. None of our drops, however, showed any evidence of a new twisted ground state such as that observed by Lavrentovich and Terentjev [19] (LT) in a different system near a transition to a smectic phase. Nevertheless, our experiments confirm the existence of a soft mode whose energy vanishes at a critical point in agreement with the calculations of RS and our analytical analysis herein.

A primary issue we address is the limit of stability of the radial hedgehog. There are two mathematical approaches to this issue that yield identical results for regions of stability but different results for normal-mode energies and associated eigenfunctions, not only in trapped hedgehogs in nematic drops but also in disclinations trapped in islands in two-dimensional freestanding smectic-C films [24–28]. The first approach, which is widespread in the literature [5,13,21,25,26,29,30], capitalizes on a special feature of these systems (see Sec. V) to produce mode energies that vanish at boundaries of stability but do not appear in measurable correlation functions. The second approach, presented here, again correctly identifies regions of stability, but also provides normal modes and associated correlation functions

that are experimentally measurable. We obtain an analytical expression for the energy of the soft mode, which vanishes when μ reaches a critical value μ_c, calculated by RS, and we present an algorithm for calculating the other modes to essentially arbitrary accuracy. This analysis represents a surprisingly complex application of partial differential equations with eigenfunctions composed of Bessel functions with irrational and/or complex indices.

The remainder of this paper is organized as follows: Section II defines the system under consideration, briefly reviews the Frank elastic energy of NLCs, and adapts the latter to the spherical-drop geometry. Then, it outlines steps toward diagonalizing the harmonic Frank energy and finally discusses properties of the critical mode whose energy passes through zero to become negative at μ_c, indicating an instability toward a phase transition to a nonradial hedgehog state containing twist (as conjectured by RS) as well as bend in addition to splay. Section III derives general expressions for dynamic director correlation functions. Section IV derives expressions for experimentally measured correlation functions from the general expressions derived in Sec. III and discusses how the unobservably small R_1 is extracted from experimental data. Section V discusses the relationship between our full 3D calculations and the effectively 1D calculations used by RS [5,13] and others [21,25,26,29,30]. Section VI presents some concluding remarks, including a comparison between our study and that of LT [19]. Finally, there are two appendices: Appendix A is devoted to details of the calculations of mode energies and correlations functions, and Appendix B deals with how director correlation functions are extracted from experimental scattering data.

II. FRANK ENERGY OF A NEMATIC DROP

A. Model energy

In the model we use, each drop consists of two concentric spheres, the smaller with radius R_1 and the larger with radius R_2. An NLC fills the space between the two spheres whose surfaces are covered with especially prepared surfactants [12] that enforce rigid alignment of the nematogens parallel to the local radius vector, i.e., they impose perpendicular boundary conditions. Any motion of the spheres, including that of the inner sphere relative to the center of mass of the outer one, is neglected. This is the model used by RS [5,13] in their calculation of the stability limit of the radial hedgehog. It was inspired by early research on nematic emulsions [11] containing the especially prepared surfactant [12]. Important output of this research was the observation of two simple (and many more complex) configurations in similar sized drops filled with the same NLC: one, which was associated with the existence of a central droplet, exhibited a clean equilibrium radial hedgehog throughout each drop, and the second, which was associated with the absence of the central droplet, exhibits a lower-energy twisted structure. As we shall see, the existence of the soft excitation mode about the radial state of particular interest to us depends on both boundary conditions and on the values of the Frank constant elastic constants. Though our model is designed to examine the stability of the radial state in the neighborhood of a transition to a lower-energy twisted state, it also describes systems in which there is no instability.

The NLC is described by the usual Frank elastic energy,

$$F = \frac{1}{2}\int d^3r\{K_1(\nabla\cdot\mathbf{n})^2 + K_2(\mathbf{n}\cdot\nabla\times\mathbf{n})^2 + K_3[\mathbf{n}\times(\nabla\times\mathbf{n})]^2\}. \tag{1}$$

The established values for the Frank elastic constants of the NLC, 5CB, used in our experiments are $K_1 = 6.4\,\text{pN}$, $K_2 = 4.0\,\text{pN}$, and $K_3 = 10\,\text{pN}$. The radii R_1 and R_2 in our experiments varied from sample to sample. For illustration purposes in figures and tables, we use $R_1 = 5.435$ nm and $R_2 = 3.78$ μm (so that the ratio $\mu \approx 695$ is close to its critical value, see below) throughout this paper unless indicated otherwise.

With the rigid homeotropic anchoring we are assuming, the nematic director $\mathbf{n}$ is fixed at the inner and outer spheres but it can fluctuate between them. In equilibrium, $\mathbf{n}$ is homogeneously radial, $\mathbf{n} = \hat{e}_r$. To study the fluctuations about this ground state, it is useful to employ spherical coordinates and to write the director as

$$\mathbf{n} = \sqrt{1 - f^2 - g^2}\,\hat{e}_r + f\,\hat{e}_\phi + g\,\hat{e}_\theta, \tag{2}$$

where f and g are *dimensionless* functions depending on the position vector $\mathbf{r}$, which in polar coordinates is parametrized by the radius r, the polar angle θ, and the azimuthal angle ϕ. Insertion of Eq. (2) into Eq. (1) converts F to a nonlinear functional of the two-dimensional vector $\psi(\mathbf{r}) = (f(\mathbf{r}), g(\mathbf{r}))$. In the harmonic limit, excitation energies are determined by the eigenvalue problem:

$$\frac{\delta F}{\delta\psi(\mathbf{r})} = D\psi, \quad \text{and} \quad D\psi_q = \varepsilon_q\psi_q(\mathbf{r}), \tag{3}$$

where the kernel D is a matrix differential operator with dimension of energy density, $q = \{mln\}$ is the eigenfunction index, ε_q is the q-eigenvalue with units of energy density, and ψ_q is the eigenfunction that because its equation is linear can have any units. We choose, however, to normalize ψ_q so that it has units of (volume)$^{-1/2}$. Static correlation functions are completely determined by the full set of ε_q and ψ_q. Because f and g are periodic in ϕ, it is natural to expand them in a Fourier series in ϕ:

$$f(r,\theta,\phi) = \frac{1}{\sqrt{2\pi}}\sum_{m=-\infty}^{\infty} f_m(r,\theta)e^{im\phi}, \tag{4a}$$

$$g(r,\theta,\phi) = \frac{1}{\sqrt{2\pi}}\sum_{m=-\infty}^{\infty} g_m(r,\theta)e^{im\phi}. \tag{4b}$$

Because both f and g are real, their Fourier coefficients have the property that $f_m^* = f_{-m}$ and $g_m^* = g_{-m}$ for $|m| > 0$.

Next, we use the functions f_m and g_m, Eq. (2), to recast the Frank energy Eq. (1) in spherical coordinates. After a fair

amount of algebra, we arrive at

$$F = \frac{1}{2}\int_{R_1}^{R_2} dr r^2 \int_{-1}^{1} dx\,(f_0, g_0) D_0 \begin{pmatrix} f_0 \\ g_0 \end{pmatrix} + \sum_{m>0} \int_{R_1}^{R_2} dr r^2 \int_{-1}^{1} dx\,(f_{-m}, g_{-m}) D_m \begin{pmatrix} f_m \\ g_m \end{pmatrix}, \tag{5}$$

where we have dropped a constant term corresponding to the Frank energy, $8\pi K_1(R_2 - R_1)$, of the equilibrium radial hedgehog. The variable x is defined as $x = \cos(\theta)$. The kernel is

$$D_m = \begin{pmatrix} D_m^{ff} & D_m^{fg} \\ D_m^{gf} & D_m^{gg} \end{pmatrix}, \tag{6}$$

where

$$D_m^{ff} = \frac{1}{r^2} K_3 \big[D^r - 2\beta_1 + \beta_2 D^x_{p^f(m)} \big], \tag{7a}$$

$$D_m^{gg} = \frac{1}{r^2} K_3 \big[D^r - 2\beta_1 + \beta_1 D^x_{p^g(m)} \big], \tag{7b}$$

$$D_m^{fg} = -i\,m\,\frac{K_1}{r^2} \Big[(1+\eta_2)\frac{x}{1-x^2} - (1-\eta_2)\partial_x \Big], \tag{7c}$$

$$D_m^{gf} = i\,m\,\frac{K_1}{r^2} \Big[(1+\eta_2)\frac{x}{1-x^2} + (1-\eta_2)\partial_x \Big], \tag{7d}$$

and D_0 is simply $D_{m=0}$. Note that every component of the D-matrices has a leading coefficient of $1/r^2$. Here and in the following, we make use of the abbreviations

$$\beta_1 = K_1/K_3, \quad \beta_2 = K_2/K_3, \tag{8a}$$

$$\eta_2 = K_2/K_1, \quad \eta_3 = K_3/K_1, \tag{8b}$$

$$p^f(m) = \sqrt{1 + m^2/\eta_2}, \quad p^g(m) = \sqrt{1 + m^2\eta_2}. \tag{8c}$$

The differential operators appearing in the diagonal elements are defined as

$$D^r = -r^2\partial_r^2 - 2r\partial_r, \tag{9a}$$

$$D^x_p = -(1-x^2)\partial_x^2 + 2x\partial_x + \frac{p^2}{1-x^2}, \tag{9b}$$

each of which is homogeneous in r (i.e., invariant under $r \to \xi r$ for any ξ) and dimensionless. Recall that D^ψ and thus $D^{\chi\chi'}$ for $\chi, \chi' = f, g$ has units of energy density, implying that D^x_p and D^r are dimensionless because the Frank constants have units of (energy/length). Here, and occasionally in the following, we use p as a shorthand for both $p^f(m)$ and $p^g(m)$. Note that D_m is Hermitian, and hence its eigenvalues are guaranteed to be real as they should be.

B. Eigensystem

The Frank energy densities of our hedgehog are the eigenvalues of D_m, whose exact evaluations are prohibitively difficult, except in the case $m = 0$ for which the off-diagonal components of D_m vanish. Thus, for $m > 0$, we resort to a perturbative approach where we initially ignore the cross-terms D_m^{fg} and D_m^{gf} and determine the eigenvalues and eigenfunctions of the diagonal elements D_m^{ff} and D_m^{gg} only. Then, we expand the entire Frank energy (including the cross-terms) in terms of these eigenvalues and eigenfunctions up to some practical order. This will provide us with truncated energy matrices that will allow us to calculate measurable quantities such as director correlation functions approximately.

Examining D_m^{ff} and D_m^{gg}, we note that their x-dependence is contained entirely in D^x_p. This structure motivates a product ansatz of the form

$$f_m(r,x) = \sum_{ln} A_{mln}\, u^f_{mln}(r)\, v_{p^f(m),l}(x), \tag{10a}$$

$$g_m(r,x) = \sum_{ln} B_{mln}\, u^g_{mln}(r)\, v_{p^g(m),l}(x), \tag{10b}$$

with expansion coefficients A_{mln} and B_{mln}. f_m and g_m are unitless as is v_p. Below we will define u^f and u^g to have units of (volume)$^{-1/2}$ so that the A and B coefficients have units of (volume)$^{1/2}$. Because f and g are real, these coefficients satisfy $A^*_{mln} = A_{(-m)ln}$ and $B^*_{mln} = B_{(-m)ln}$.

The eigenvalue equations for $v_{p,l}$ are given by

$$D^x_p\, v_{p,l}(x) = \varepsilon^x_{p,l}\, v_{p,l}(x), \tag{11}$$

which is identical in form to the general Legendre equation governing the associated Legendre polynomials with one important distinction: The integer valued index for the order of the polynomial is replaced in our hedgehog problem by $p(m)$ whose values are in general irrational numbers. Nonetheless, our equation can be solved using standard methods, and the resulting eigenvalues read

$$\varepsilon^x_{p,l} = (l+p)(l+1+p), \tag{12}$$

with

$$v_{p,l}(x) = \mathrm{X}^{-1}_{p,l}(1-x^2)^{p/2}\Pi^p_l \tag{13}$$

as the corresponding eigenfunctions. Here, the $\mathrm{X}_{p,l}$ are normalization factors and the Π^p_l are polynomials of degree l. The first few of these Legendre polynomials read

$$\Pi^p_0 = 1, \tag{14a}$$

$$\Pi^p_1 = x, \tag{14b}$$

$$\Pi^p_2 = 1 - (2p+3)x^2, \tag{14c}$$

$$\Pi^p_3 = x - \tfrac{1}{3}(2p+5)x^3, \tag{14d}$$

$$\Pi^p_4 = 1 - (4p+10)x^2 + \tfrac{1}{3}(2p+5)(2p+7)x^4. \tag{14e}$$

Note that the $v_{p,l}$ satisfy the usual orthonormality and completeness relations.

Next, we turn to the radial eigenvalue equations. Using Eqs. (7a) and (7b), with help from Eq. (11), we obtain

$$\frac{1}{r^2} K_3 \big[D^r - 2\beta_1 + \beta_2\, \varepsilon^x_{p^f(m),l} \big] u^f_{mln}(r) = \varepsilon^f_{mln} u^f_{mln}(r), \tag{15a}$$

$$\frac{1}{r^2} K_3 \big[D^r - 2\beta_1 + \beta_1\, \varepsilon^x_{p^g(m),l} \big] u^g_{mln}(r) = \varepsilon^g_{mln} u^g_{mln}(r). \tag{15b}$$

The left-hand side of both equations have an explicit prefactor of r^{-2}; both right-hand sides do not. If we are only interested in zero eigenvalues, we can remove the r^{-2} factor on the left-hand side without changing solutions. But for any nonzero eigenvalue, this factor cannot be removed. After substituting Eq. (12) into (15), and multiplying both sides by r^2, we recast

TABLE I. Select values of ν^{χ}_{ml}, the corresponding smallest zeros κ^{χ}_{ml1} and energy densities ε^{χ}_{ml1} [with units $\frac{\mathrm{Kg}}{\mathrm{m^2 s^2}}$] for our example hedgehog.

m, l	ν^{f}_{ml}	κ^{f}_{ml1}	ε^{f}_{ml1}	ν^{g}_{ml}	κ^{g}_{ml1}	ε^{f}_{ml1}
0, 0	0.4796 i	0.1723	0.0208	1/2	3.1461	6.9273
0, 1	1.1705	4.0599	11.5360	1.6763	4.7218	15.6036
0, 2	1.9417	5.0615	17.9297	2.5788	5.8613	24.0437
1, 0	0.8093	3.5727	8.9334	1.9333	3.7083	9.6243
1, 1	1.6568	4.6966	15.4377	0.9088	5.0508	17.8543
1, 2	2.3738	5.6061	21.9961	2.8159	6.1542	26.5071

the latter as

$$\left[r^2\partial_r^2 + 2r\partial_r + \left(k^{\chi}_{mln}\right)^2 r^2 + 2\beta_1 - \lambda^{\chi}_{ml}\right]u^{\chi}_{mln}(r) = 0, \quad (16)$$

where χ is a placeholder for f or g,

$$k^{\chi}_{mln} = \sqrt{\frac{\varepsilon^{\chi}_{mln}}{K_3}}, \quad (17)$$

and

$$\lambda^{f}_{ml} = \beta_2\, \varepsilon^{x}_{p^f(m),l}, \quad \lambda^{g}_{ml} = \beta_1\, \varepsilon^{x}_{p^g(m),l}. \quad (18)$$

Note that all terms in Eq. (16) are homogeneous in r except the term $(k^{\chi}_{klm})^2 r^2$ arising from the right-hand sides of Eq. (15). To further simplify this differential equation, we set

$$u^{\chi}_{mln}(r) = \frac{Z_{\nu^{\chi}_{ml}}(k^{\chi}_{mln} r)}{\sqrt{V^{\chi}_{mln}}\sqrt{k^{\chi}_{mln} r}}. \quad (19)$$

Here, we have included in the denominator a factor $\sqrt{V^{\chi}_{mln}}$ for normalization purposes, where V^{χ}_{mln} is a volume that we will determine further below. Inserting Eq. (19) into Eq. (16), we obtain

$$\left[r^2\partial_r^2 + r\partial_r + r^2 - \left(\nu^{\chi}_{ml}\right)^2\right]Z_{\nu^{\chi}_{ml}}(r) = 0, \quad (20)$$

where

$$\nu^{\chi}_{ml} = \sqrt{\lambda^{\chi}_{ml} + 1/4 - 2\beta_1}. \quad (21)$$

All λ^{χ}_{ml} are real, so the ν^{χ}_{ml}, being the square roots of real numbers, are either pure real or pure imaginary, as discussed above, depending on the argument of the square root. For our experimental Frank constants, cf. Table I, all ν^{χ}_{ml} are real except for

$$\nu^{f}_{00} = i\sqrt{2\beta_1 - 2\beta_2 - \tfrac{1}{4}}, \quad (22)$$

which is pure imaginary. For future reference, it is convenient to introduce

$$\omega(\beta_1, \beta_2) = e^{i\pi/\nu^{f}_{00}}, \quad (23)$$

which is pure real because ν^{f}_{00} is pure imaginary.

Equation (20) is the well-known Bessel differential equation. Its solutions are the Bessel functions of the first and second kind, respectively, $J_\nu(r)$ and $Y_\nu(r)$, and linear combinations thereof. For our hedgehog problem, the index ν of these Bessel function takes on the values given by the ν^{χ}_{ml} which are pure real (either irrational or rational, e.g., $\nu^{g}_{00} = 1/2$) or pure imaginary as is the case for ν^{f}_{00}— see above. When ν is imaginary, $J_\nu(r)$, and $Y_\nu(r)$ are, in general, complex valued functions. Thus, care must be taken to ensure that our solution for $u^{\chi}_{00n}(r)$ be real valued. Furthermore, we need to construct our solution so that the homeotropic boundary conditions are satisfied: $u^{\chi}_{mln}(R_1) = u^{\chi}_{mln}(R_2) = 0$. A linear combination of Bessel functions that both makes $u^{f}_{00n}(r)$ real and guarantees that $u^{\chi}_{mln}(R_1) = 0$ by construction is

$$Z_\nu(kr) = Y_\nu(kr)J_\nu(kR_1) - J_\nu(kr)Y_\nu(kR_1). \quad (24)$$

The boundary condition at the outer sphere is enforced by choosing k so that $Z_\nu(kR_2) = 0$, or in other words, by calculating the zeros of $Z_\nu(\kappa)$, where

$$\kappa = kR_2. \quad (25)$$

Note that $Z_\nu(\kappa)$ depends on the ratio of radii,

$$\mu = R_2/R_1, \quad (26)$$

but not on R_1 or R_2 individually. Except for one special case, $Z_\nu(\kappa)$ for each ν has infinitely many real positive zeros,

$$\kappa^{\chi}_{mln} = k^{\chi}_{mln} R_2, \quad (27)$$

labeled in ascending order by $n = 1, 2, 3, \ldots$ (for fixed χ, m and l). Figure 1 plots κ^{f}_{mln} for the lowest-energy 001, 011 and 002 modes as a function of μ for a system with the Frank constants of the material in our experiments.

The special case involves the 001 mode of f. When ν^{f}_{00} is imaginary, κ^{f}_{001} is real and positive for μ less than a critical value μ_c at which point it vanishes. When $\mu > \mu_c$, $\overline{\kappa}^{f}_{001} \equiv \kappa^{f}_{001}/i$ is real and grows from zero at $\mu = \mu_c$. These zeros determine the values of the quantities defined in Eq. (17), which we refer to somewhat casually as wavenumbers. Consequently the "quantized" eigenenergy densities are

$$\varepsilon^{\chi}_{mln} = K_3\left(\frac{\kappa^{\chi}_{mln}}{R_2}\right)^2. \quad (28)$$

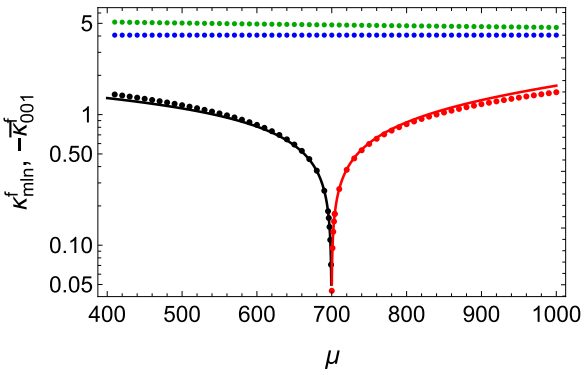

FIG. 1. Semilog plot of κ for the three lowest-energy azimuthal modes (indicated by the superscript f): Black dots and black line for κ^{f}_{001} for $\mu < \mu_c$; red dots and red line for $\overline{\kappa}^{f}_{001} = \kappa^{f}_{001}/i$ for $\mu > \mu_c$; blue dots for κ^{f}_{002}, and green dots for κ^{f}_{011}. The black and red lines are obtained from the analytical expression of Eq. (48). See Fig. 8 for a plot of the energy density.

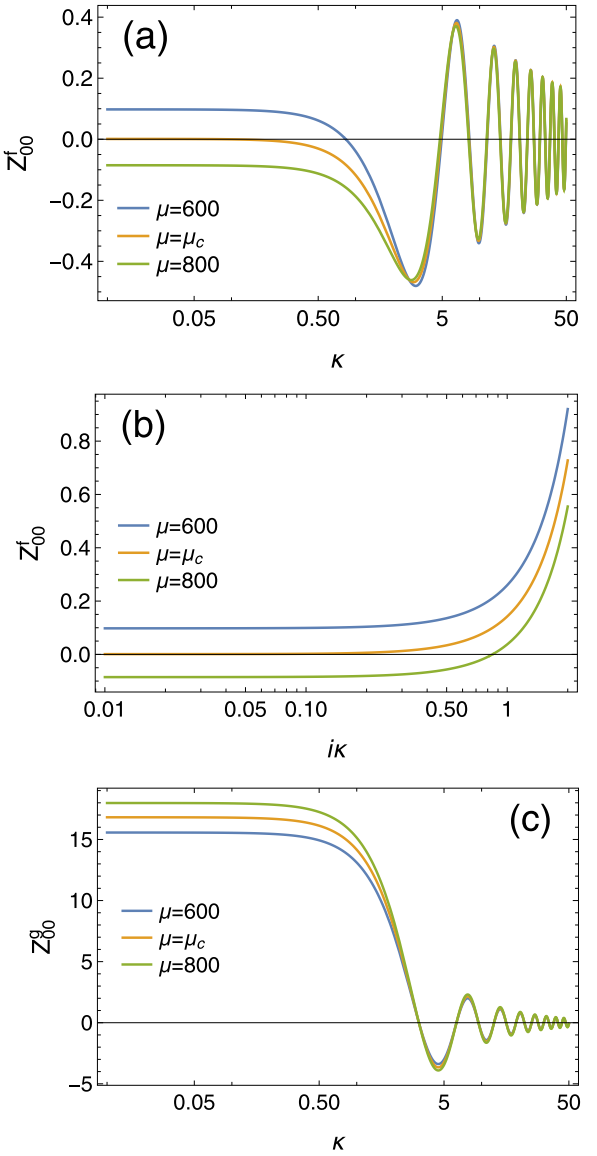

FIG. 2. Plots of $Z^{\chi}_{00} \equiv Z_{\nu^{\chi}_{00}}$, whose zeros determine k^{χ}_{00n}, of our experimental hedgehog with $\nu^f_{00} = 0.4796\,i$ and $\nu^g_{00} = 1/2$ for $\mu < \mu_c$, $\mu = \mu_c$ and $\mu > \mu_c$. (a) For real κ, Z^f_{00} has a zero at small κ that approaches the origin as $\mu \to \mu_c^-$ and then disappears for $\mu > \mu_c$ while the zeros of the higher modes (002, 003, etc.) remain almost unchanged. (b) For imaginary κ, Z^f_{00} is a monotonically increasing function that has a zero only if $\mu \geqslant \mu_c$. (c) Z^g_{00} with real κ has a large value at $\kappa = 0$, and there is no zero near the origin. The rapid oscillations in panels (a) and (c) are a consequence of the logarithmic scale.

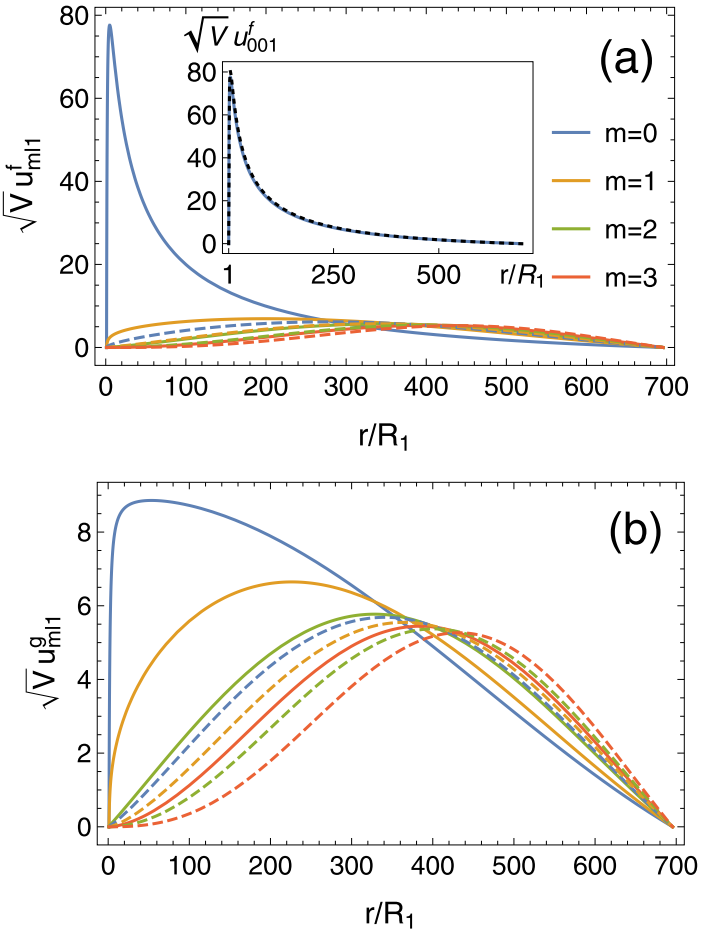

FIG. 3. Radial eigenfunctions (a) u^f_{ml1} and (b) u^g_{ml1}. V is the total volume of the drop given by $V = \frac{4\pi}{3}R_2^3$. The colored lines refer to $\mu = 695 < \mu_c$ for $l = 0$ (solid) and $l = 1$ (dashed). The inset to (a) shows the dominant radial eigenfunction u^f_{001} for $\mu = 695 < \mu_c$ (blue line) and $\mu = 710 > \mu_c$ (black dots). The plots of this function for values of μ just below and above μ_c are sharply peaked near the core and almost indistinguishable.

Thus, all ε^{χ}_{mln} are positive except ε^f_{001} when ν^f_{00} is imaginary when $\mu > \mu_c$. Figure 2 shows the graphs of (a) $Z_{\nu^f_{00}}(\kappa)$, (b) $Z_{\nu^f_{00}}(i\overline{\kappa})$, and (c) $Z_{\nu^g_{00}}(\kappa)$. Note that $Z_{\nu^f_{00}}(\kappa)$ oscillates and, as a result, has an infinite number of zeros including that of the critical mode that approaches zero as $\mu \to \mu_c^-$. When $\mu > \mu_c$, there is no zero of $Z_{\nu^f_{00}}(\kappa)$ at $\kappa = 0$ as $\mu \to \mu_c^+$, and as a result no critical mode arising from this function. However, $Z_{\nu^f_{00}}(i\overline{\kappa})$ does not oscillate. At $\overline{\kappa} = 0$, it passes from greater than to less than zero as μ passes from greater than to less than μ_c, yielding a single mode that disappears when μ passes through zero. This mode with $\kappa^2_{001} < 0$ is a continuation to $\mu > \mu_c$ of the critical mode for $\mu < \mu_c$ as shown in Fig. 1.

The height of $Z_{\nu^g_{00}}(0)$ and the position of the zeros of $Z_{\nu^g_{00}}(\kappa)$ change very little with variations in μ, and no zeros exist below a critical value of κ. Thus, the 001 mode of f is the only critical mode in the system, and all others, including those associated with g, can be ignored near the critical point. We can, therefore, assume that near $\mu = \mu_c^-$, f is proportional to the 001 wave function, which according to Eq. (10) is proportional to $\cos\theta\, u^f_{001}(r)$, where the radial part is strongly peaked in the vicinity of the core as shown in Fig. 3. To linear order, the director is $\mathbf{n} \approx \hat{e}_r + f(r,\theta)\hat{e}_\phi$, which describes a state with "twist" regardless of the functional form of f and one with "bend" so long as f is not inversely proportional to r:

$$\mathbf{n}\cdot\nabla\times\mathbf{n} \sim \cos\theta\, u^f_{001}$$
$$\mathbf{n}\times(\nabla\times\mathbf{n}) \sim -\frac{1}{r}\hat{e}_\phi \sin\theta\, \partial_r\big[r u^f_{001}(r)\big]. \qquad (29)$$

For this reason, we use the term "twist-bend" hedgehog to describe the state for μ just above μ_c. As μ increases beyond μ_c, the director pattern will change while maintaining an overall hedgehog charge of $+1$.

Next, we turn to the volume V^{χ}_{mln} introduced in Eq. (19). For our $u^{\chi}_{mln}(r)$ to satisfy the orthonormality relations

$$\int_{R_1}^{R_2} dr r^2 u^{\chi}_{mln}(r) u^{\chi}_{mln'}(r) = \delta_{nn'}, \tag{30}$$

we set

$$V^{\chi}_{mln} = \left(\frac{R_2}{\kappa^{\chi}_{mln}}\right)^3 \gamma^{\chi}_{mln}, \tag{31}$$

where

$$\gamma^{\chi}_{mln} = \int_{\kappa^{\chi}_{mln}/\mu}^{\kappa^{\chi}_{mln}} dy y Z^2_{\nu^{\chi}_{ml}}(y) \tag{32}$$

is a dimensionless integral depending on κ^{χ}_{mln} and the ratio of radii μ.

Note that, at this point, we have completely determined all radial eigenfunctions $u^{\chi}_{mln}(r)$ for which we have calculated the corresponding κ^{χ}_{mln}. Figure 3 shows plots of u^{f}_{mln} and u^{g}_{mln} for various values of mln. Note that the lowest energy curves u^{f}_{001} and u^{g}_{001} are peaked near the origin, but u^{f}_{001} strongly so.

Finally, we can write down expansions of the functions f and g in terms of the solution of the azimuthal and radial eigenvalue problems. Combining the Fourier series of Eq. (4) with Eq. (10), we obtain

$$f(\vec{r}) = \sum_{mln} A_{mln} \Psi^{f}_{mln}(\vec{r}), \tag{33a}$$

$$g(\vec{r}) = \sum_{mln} B_{mln} \Psi^{g}_{mln}(\vec{r}), \tag{33b}$$

where $\vec{r} = (r, x, \phi)$ and

$$\Psi^{\chi}_{mln}(\vec{r}) = \frac{1}{\sqrt{2\pi}} u^{\chi}_{mln}(r)\, v^{\chi}_{ml}(x)\, e^{im\phi}, \tag{34}$$

with

$$v^{\chi}_{ml}(x) = v_{p^{\chi}(m),l}. \tag{35}$$

Note that the product eigenfunctions as a whole satisfy the orthonormality relations

$$\int d\vec{r}\ \Psi^{\chi *}_{mln}(\vec{r}) \Psi^{\chi}_{m'l'n'}(\vec{r}) = \delta_{mm'}\delta_{ll'}\delta_{nn'}, \tag{36}$$

where we introduced the shorthand

$$\int d\vec{r} = \int_{R_1}^{R_2} dr r^2 \int_{-1}^{1} dx \int_{0}^{2\pi} d\phi, \tag{37}$$

and that A_{mln} and B_{mln} have units of square root of volume.

C. Expansion of the Frank energy

As announced above, we are next going to expand the Frank energy in terms of the eigenfunctions calculated in the previous section. Because these eigenfunctions are eigenfunctions of their respective diagonal element of D_m only, the cross-terms in Eq. (5) require some extra consideration.

Insertion of our eigenfunctions into Eq. (5) produces the integrals

$$\int d\vec{r}\ \Psi^{f*}_{mln}(\vec{r})\, D^{fg}_{m}\, \Psi^{g}_{m'l'n'}(\vec{r}) = -im\,\delta_{mm'}\Theta_{mll'nn'}, \tag{38a}$$

$$\int d\vec{r}\ \Psi^{g*}_{mln}(\vec{r})\, D^{gf}_{m}\, \Psi^{f}_{m'l'n'}(\vec{r}) = im\,\delta_{mm'}\Theta_{ml'ln'n}. \tag{38b}$$

The right-hand sides of Eq. (38) are proportional to $\delta_{mm'}$ because D^{fg}_m and D^{gf}_m are independent of ϕ. They are not diagonal in l because of the x-dependence of D^{fg}_m and D^{gf}_m, which leads to the integral

$$\Lambda_{mll'} = \int_{-1}^{1} dx\, v^{f}_{ml}(x)\, D^{fg}_{m}\, v^{g}_{ml'}(x). \tag{39}$$

They are also not diagonal in n because the orthogonality relation in Eq. (30) only applies when $\chi = f$ (or $\chi = g$) in both functions $u^{\chi}_{mln}(r)$ in the integrand, but not for the case that mixes f and g, which leads to the integral

$$\Omega_{mll'nn'} = \frac{R_2}{\kappa^{f}_{mln}} \int_{\kappa^{f}_{mln}/\mu}^{\kappa^{f}_{mln}} dy y^{-1} \frac{Z_{\nu^{f}_{ml}}(y)}{\sqrt{V^{f}_{mln}}} \frac{Z_{\nu^{g}_{ml'}}\left(\frac{\kappa^{g}_{ml'n'}}{\kappa^{f}_{mln}} y\right)}{\sqrt{V^{g}_{mln}}}. \tag{40}$$

Overall, we have

$$\Theta_{mll'nn'} = K_1 \Lambda_{mll'} \Omega_{mll'nn'}. \tag{41}$$

With this in mind, we are now in the position to write down the desired expansion of the Frank energy. Collecting, we get

$$\begin{aligned} F = \frac{1}{2} \sum_{ln} \left[A^2_{0ln}\varepsilon^{f}_{0ln} + B^2_{0ln}\varepsilon^{g}_{0ln}\right] \\ + \sum_{m>0,ln} \left[|A_{mln}|^2 \varepsilon^{f}_{mln} + |B_{mln}|^2 \varepsilon^{g}_{mln}\right] \\ + \sum_{m>0,ll'nn'} \left[-im A^{*}_{mln} B_{ml'n'}\, \Theta_{mll'nn'} \right. \\ \left. + im B^{*}_{mln} A_{ml'n'}\, \Theta_{ml'ln'n}\right]. \end{aligned} \tag{42}$$

Clearly the f and g modes with $m = 0$ but arbitrary ln do not couple, but those with $m > 0$ do. In Appendix A, we will discuss an approximation procedure for diagonalizing the $m \neq 0$ part of the F. In the meantime, we will mostly focus on the experimentally relevant $m = 0$ f-states.

D. The critical mode

As a corollary of the results derived in the previous section, we can readily assess the stability of our hedgehog. The radial equilibrium conformation is stable when the eigenvalues of the kernel defined in Eq. (6) are positive. Stability is lost when the smallest eigenvalue, corresponding to $(m, l, n) = (0, 0, 1)$, becomes negative. We have learned that the off-diagonal parts D^{fg} and D^{gf} of the kernel vanish for $m = 0$. Thus, the stability of the radial hedgehog is governed by ε^{f}_{001} and ε^{g}_{001}. Recall from Eq. (28) that these eigenvalues are proportional to the square of the smallest zeros κ^{χ}_{001} of the functions $Z_{\nu^{\chi}_{00}}(\kappa)$ depicted in Fig. 2. The value of $Z_{\nu^{g}_{00}}(0)$ changes little as μ changes, but when ν^{f}_{00} is imaginary, the

value of $Z_{\nu_{00}^f}(0)$ passes through zero and changes sign at a critical value of μ. As a result, the value of κ_{001}^f approaches zero as the height $Z_{\nu_{00}^f}(0)$ approaches zero. The height of $Z_\nu(0)$ for any ν is given by the zeroth order of its expansion about $\kappa = 0$,

$$Z_\nu(\kappa) - \mathcal{O}(\kappa^2) = \frac{\mu^\nu - \mu^{-\nu}}{\pi\nu} \to \frac{1}{\pi\nu_{00}^f}(e^{i\pi \ln\mu/\ln\omega} - e^{-i\pi\ln\mu/\ln\omega}), \quad (43)$$

which vanishes at

$$\ln\mu = \ln\omega(\beta_1,\beta_2) = \frac{i\pi}{\nu_{00}^f} \equiv \ln\mu_c, \quad (44)$$

defining a critical μ, which is real because ω is. For the values of Frank constants in our experiments,

$$\mu_c^f \equiv \mu_c = \exp\left(\frac{i\pi}{\nu_{00}^f}\right) = 699.715. \quad (45)$$

Using Eq. (22), we find that the condition for the vanishing of ε_{00}^f is

$$\left(\nu_{00}^f\right)^2 = 2\beta_2 - 2\beta_1 + \frac{1}{4} = -\left(\frac{\pi}{\ln\mu}\right)^2 \quad \text{or}$$
$$-2K_1 + 2K_2 + K_3\left[\frac{1}{4} + \left(\frac{\pi}{\ln\mu}\right)^2\right] = 0. \quad (46)$$

Equation (46) is identical to the limit of stability calculated by RS, and at $\mu \to \infty$, it is identical to the limit of stability of a hedgehog trapped in a sphere without an inner sphere, set by mathematical inequalities in Ref. [31]. It defines a surface in the space of β_1, β_2, and μ on which ε_{00}^f vanishes. Here we mostly focus on the case in which β_1 and β_2 are fixed so that Eq. (46) [or equivalently Eq. (45)] defines the critical ratio μ_c. Of course, if μ is fixed, it constrains the value of β_1 and β_2.

Equations (45) and (46) impose two constraints on ν_{00}^f that together require the inequalities

$$0 > \left(\nu_{00}^f\right)^2 > -\left(\frac{\pi}{\ln\mu}\right)^2 \quad (47)$$

be satisfied because ν_{00}^f must be imaginary and $(\kappa_{001})^2$ and ε_{001}^f must be positive in order for the soft mode to exist and for the radial hedgehog to be stable. We will present an alternative direct derivation of this result in Sec. V. Equation (47) restricts the range of Frank constants at fixed μ for which the soft mode exists and the radial hedgehog state is stable.

The $R_1 \to 0$ limit has some interesting properties. It causes μ to become infinite without affecting the outer boundary that imposes the existence of a trapped hedgehog or topologically equivalent structure (e.g., a strength $+1/2$ disclination ring), and it removes any constraints on the stability of the radial hedgehog arising from the inner droplet. In other words, this limit has the same effect as removing the inner droplet altogether [5,13], leading to stability for the radial hedgehog only if $-2\beta_1 + 2\beta_2 + (1/4) = (\nu_{00}^f)^2 > 0$. An interpretation of this result is that the bulk energy [Eq. (1)] determines the stability of the radial hedgehog in the absence of the central droplet. When a droplet is present, it introduces surface constraints that open a region of radial stability that is opposed by the bulk energy. The soft mode only exists in systems in which the radial hedgehog cannot be stable without the surface constraints.

We have just shown that the lowest excitation energy vanishes when $\mu = \mu_c$. It is instructive to see how κ_{001}^f and thus ε_{001}^f changes as μ_c is approached. For μ near μ_c, κ_{001}^f approaches zero at μ_c, and we can find an approximate solution for it by extending the expansion of Eq. (43) to quadratic order and solving for its zero in terms of κ^2. The result is

$$\kappa^2(\mu) = \frac{4\mu^2(1-\nu^2)(1-\mu^{2\nu})}{(\mu^2+1)(1-\mu^{2\nu}) + \nu(\mu^2-1)(1+\mu^{2\nu})}, \quad (48)$$

where we abbreviated $\kappa = \kappa_{001}^f$ and $\nu = \nu_{00}^f$. Equation (48) will be useful in discussing the connection of our theoretical findings to our experimental data, see Sec. IV B. It encapsulates the behavior of κ for small $|\kappa|$. When ν_{001}^f is real, Eq. (48) has no zero and κ remains real and positive for all μ. When ν_{00}^f is imaginary, κ does reach zero at μ_c. For $\mu < \mu_c$, $\kappa_{001} \sim \sqrt{\mu_c - \mu}$, implying linear behavior of κ_{001}^2 near $\mu = \mu_c$. When $\mu > \mu_c$, $\kappa_{001} \equiv i\bar{\kappa}_{001} \sim i\sqrt{\mu - \mu_c}$ is imaginary, implying a negative value for $\kappa_{001}^2 \sim -(\mu - \mu_c)$ and for ε_{001} in Eq. (28). This signals an instability toward a phase transition to a new ground state for $\mu > \mu_c$. Figure 1 shows the three smallest κ (κ_{001}^f, κ_{002}^f, and κ_{011}^f) as functions of μ. The dots in this plot stem from computing the smallest zeros of the functions $Z_\nu(\kappa)$, cf. Eq. (24), numerically. The black curve for $\mu < \mu_c$ and the red curve for $\mu > \mu_c$ in Fig. 1 are both obtained from Eq. (48), and comparison to the black and red dots shows that it provides an excellent approximation over a fairly broad range of μ's. Note that the values of κ_{002}^f and κ_{011}^f are insensitive to the transition.

In general, the core radius R_1 is a parameter that must be specified based on supplied information, e.g., from measurements, rather than by a prediction of our theory. The situation is different, however, for critical hedgehogs with $\mu = \mu_c$. For these, Eq. (26) immediately leads to

$$R_1 = \frac{1}{\mu_c} R_2, \quad (49)$$

with small corrections for μ near μ_c. We will revisit the relation between the core and exterior radii in Sec. IV B when we interpret some of our experimental results.

III. CORRELATION FUNCTIONS

Using optical techniques, our experiments measure dynamical correlation functions of the nematic director. In this section, we derive expressions for these functions with emphasis on those associated with the azimuthal function f in the equatorial plane. Mainly, we are interested in describing the amplitude and decay of the correlation functions seen in our experiments [22]. To this end, we focus on simple over-damped, pure relaxation dynamics. A full hydrodynamic theory that would include orientational anisotropy, fluid flow, and other phenomena that affect director dynamics is beyond

the scope of the present work. To avoid needless repetition, we will for the time being explicitly write down equations only for quantities pertaining to f. It is understood that for any of these equations there is an accompanying equation pertaining to g that can be retrieved from the f equations simply by replacing f with g.

In general, simple relaxation dynamics of the azimuthal component of the director is described by

$$\partial_t f(\vec{r}) = -\Gamma \frac{\delta F}{\delta f(\vec{r})}, \tag{50}$$

where Γ is a kinetic coefficient given by the inverse of rotational viscosity γ_1 of the mesogens. Electro-optical experiments [32] and theoretical calculations [33] indicate that $\gamma_1 = 1/\Gamma$ lies in the range of about 0.5 to 1.0 poise at room temperature, which translates to Γ of about 10 to 20 $\frac{\text{ms}}{\text{Kg}}$.

It is clear from Eq. (42) that f and g do not mix when $m = 0$, greatly simplifying the arithmetic of calculating correlation functions. In this limit, Eq. (50) implies the following equations of motion for the expansion coefficients A_{0ln},

$$\partial_t A_{0ln} = -\Gamma\, \varepsilon^f_{0ln} A_{0ln}, \tag{51}$$

and similar expressions for B_{0ln}. These equations of motion are readily integrated with the result

$$A_{0ln}(t) = A_{0ln}(0)\, e^{-\Gamma\, \varepsilon^f_{0ln} t}. \tag{52}$$

This leads, after taking the thermodynamic average, to

$$\langle A_{0ln}(t) A_{0ln}(0)\rangle = \frac{k_B T}{\varepsilon^f_{0ln}} e^{-\Gamma\, \varepsilon^f_{0ln} t} = k_B T\, G^f_{0ln}(t) \tag{53}$$

for the A-A correlations, where

$$G^f_{0ln}(t) = \frac{1}{\varepsilon^f_{0ln}}\, e^{-\Gamma\, \varepsilon^f_{0ln} t}, \tag{54}$$

and $\langle ..\rangle$ signifies an average with respect to the Frank energy of Eq. (42).

Despite the complexity of the $m \neq 0$ modes, all correlation functions are invariant under the operation $\phi \to \phi + \gamma$ for any angle γ. This means that the full f correlation functions can be decomposed into a sum over components with different m's:

$$\langle f(\vec{r}, t) f(\vec{r}\,', 0)\rangle = \sum_{m=-\infty}^{\infty} S_m(r, r', x, x', t)\, e^{im(\phi-\phi')}. \tag{55}$$

$f(\vec{r}, t)$ is real so that $S_{-m} = S^*_m$ and

$$S_0(r, r', x, x', t) = \frac{k_B T}{2\pi} \sum_{ln} G^f_{0ln}(t)\, v^f_{0l}(x) v^f_{0l}(x') u^f_{0l}(r) u^f_{0l}(r') \tag{56}$$

is real. The formulas for $m \neq 0$ are presented in Appendix A.

As a corollary of our results for time-dependent correlation functions, one can readily extract results for their static counterparts. In the above, one simply has to take the limit $t \to 0$ which amounts to replacing the time-dependent G's by the corresponding inverse energy densities. Figure 4 shows the static correlation function

$$C(r, \phi) = \langle f(r, 0, \phi, 0) f(r, 0, 0, 0)\rangle \tag{57}$$

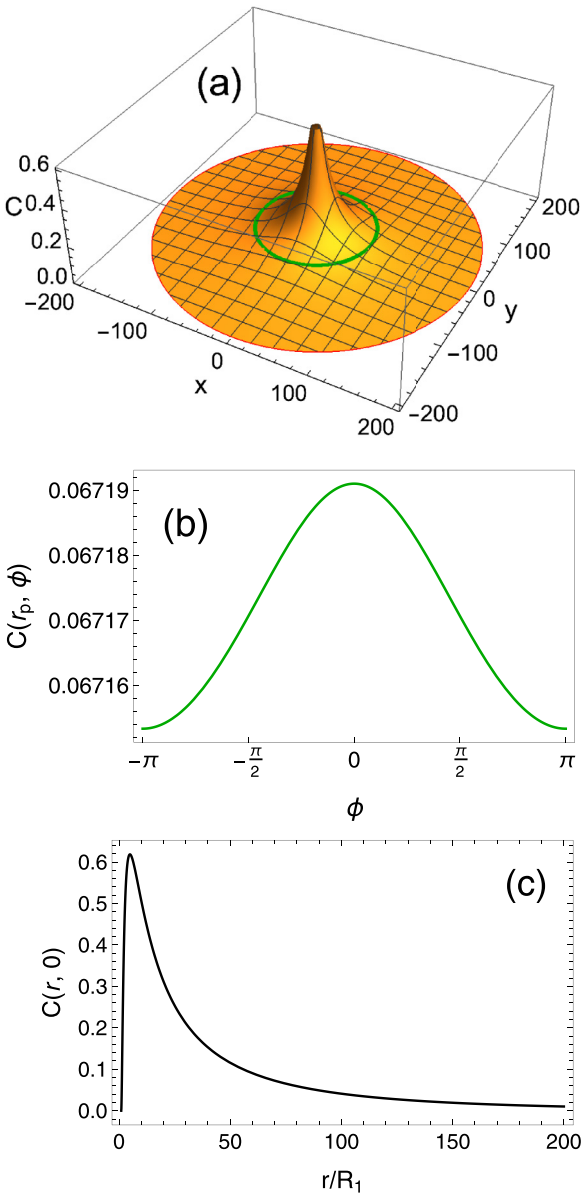

FIG. 4. The correlation function $C(r, \phi)$ defined in Eq. (57). (a) The x and y on the axis denote dimensionless coordinates in the equatorial plane and are related to r and ϕ via $r = R_1\sqrt{x^2 + y^2}$ and $\cos\phi = x/\sqrt{x^2 + y^2}$. Note that the x here must not be confused with the $x = \cos\theta$ used throughout the text. The image is cropped at $r = 200\, R_1$ to emphasize the vicinity of the core. The green loop indicates the probing radius of $r = r_p = 0.4\ \mu$m used in our measurements. (b) Zoom-in on the correlation function along the green loop. (c) Zoom-in along $\phi = 0$. Note that the correlation function vanishes at $r = R_1$ as it should. The calculations for all three subfigures included the contributions from $m = 0, 1, 2, 3$ in Eq. (55).

for two points in the equatorial plane located an angle ϕ apart on a circle about the origin. The values for the elastic constants, etc., used in this plot are those stated at the beginning of Sec. II A. Note the small variation as a function of ϕ of values of $C(r, \phi)$ in Fig. 4(b). This is a consequence of the fact that variations with ϕ require $m > 0$, which brings in higher-energy modes which yield smaller contributions to correlation functions.

IV. CONNECTION WITH EXPERIMENT

A. Experimental correlations

Having calculated theoretical predictions for correlation functions, it is useful to reflect in more detail on their precise relation to the quantities measured in our experiments. Our experiments use a crossed-polarizer setup that focuses on the equatorial plane of the drops, i.e., we use a 2D-slice approximation in which the polar angle θ is kept fixed at its equatorial value of $\pi/2$, i.e., $x = 0$. Specifically, we measure light intensity profiles that allow us to reconstruct the angle, $\delta\beta(r, \phi, t)$, that the director makes at time t with the radial direction at angle ϕ:

$$\delta\beta(r, \phi, t) = \arcsin \tilde{f}(r, \phi, t) \approx \tilde{f}(r, \phi, t), \tag{58}$$

where $\tilde{f}(r, \phi, t) = f(r, x = 0, \phi, t)$. (It is understood, as it is throughout this manuscript in our discussion of fluctuations, that f is small.)

There is an important difference between theory and experiment: the theory treats the angle ϕ as a continuous variable whereas our experiments focused on a set of $N = 4$ discrete azimuthal angles,

$$\phi_p = 2\pi \frac{p}{N}, \quad \text{where} \quad p = 0, 1, \cdots, N-1. \tag{59}$$

On the theoretical side, we show in Appendix A that although we can calculate the elements contributing to $S_m(r, r', x, x', t)$ for any reasonable choice of its indices, we do not have closed form expressions for them. Thus, we are limited in practice to a manageable number of values of the indices including m. Within our truncation scheme, however, we do have a full theoretical representation of the correlation functions that provides for a discrete Fourier transformation, which captures a certain number of discrete values of ϕ like those probed in our experiments.

Thus, the measured correlation functions in the equatorial plane ($\theta = \pi/2$, i.e., $x = 0$) are

$$\begin{aligned} C_p(r, t) &= \langle \tilde{f}(r, \phi_p, t) \tilde{f}(r, 0, 0) \rangle \\ &\approx \langle \delta\beta(r, \phi_p, t) \delta\beta(r, 0, 0) \rangle. \end{aligned} \tag{60}$$

Following Eq. (55), we furthermore deduce that

$$C_p(r, t) = \sum_{m=0}^{N-1} \tilde{S}_m(r, t)\, e^{im\phi_p}, \tag{61}$$

where we define

$$\tilde{S}_m(r, t) = \sum_{k=0}^{\infty} S_{m+kN}(r, r, 0, 0, t) \approx S_m(r, r, 0, 0, t), \tag{62}$$

which follows because $e^{im(\phi_p + kN\phi_p)} = e^{im\phi_p}$. The second approximate form follows because S_m dies off rapidly with m. Note that $\tilde{S}_m$ can be interpreted as the inverse Fourier transform of C_p,

$$\tilde{S}_m(r, t) = \frac{1}{N} \sum_{p=0}^{N-1} C_p(r, t)\, e^{-i\, m\, \phi_p} \approx S_m(r, t), \tag{63}$$

i.e., the S_m's represent the Fourier modes of the system. For our experimental setup, the dominant mode S_0 is simply given by $S_0 \approx \frac{1}{4}(C_0 + C_1 + C_2 + C_3)$. It describes the over-all (rigid) rotational diffusion of the four-leaf-clover-like pattern recorded in our experiments, cf., Fig 1 of Ref. [22]. The subdominant mode $S_1 + S_3 \approx \frac{1}{2}(C_0 - C_2)$, however, describes the "scissorlike" twist fluctuations of opposite clover leaves relative to one another. Our experimental analysis focuses mainly on the dominant mode. Collecting from above, we find that the dominant contribution to the correlation function of this mode is simply

$$S_0(r, t) = \frac{3k_B T \left[u^f_{001}(r)\right]^2}{8\pi\, \varepsilon^f_{001}} e^{-t/\tau_0}, \tag{64}$$

with a decay time

$$\tau_0 = \frac{1}{\Gamma\, \varepsilon^f_{001}}. \tag{65}$$

Note that $S_0(r, t)$ is a function of κ and μ through ε^f_{001} [Eq. (28)] and $u^f_{001}(r)$ [Eq. (19)], and τ_0 is a function of κ through ε^f_{001}. Figure 5 shows our experimental data for the amplitude $S_0 = S_0(r_{\text{probe}}, 0)$ of the correlation function and the relaxation time $\tau_0(r_{\text{probe}})$ at probing radius $r_{\text{probe}} = 0.4\,\mu$m and $t = 0$.

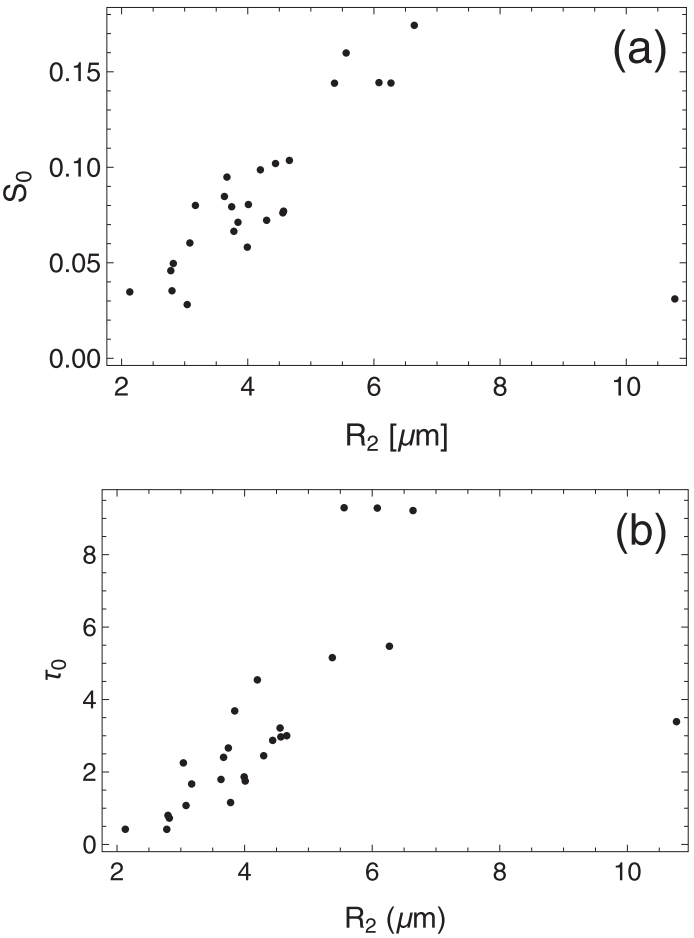

FIG. 5. Experimental data of drops displaying giant fluctuations. (a) Amplitude and (b) decay time of the dominant correlation function.

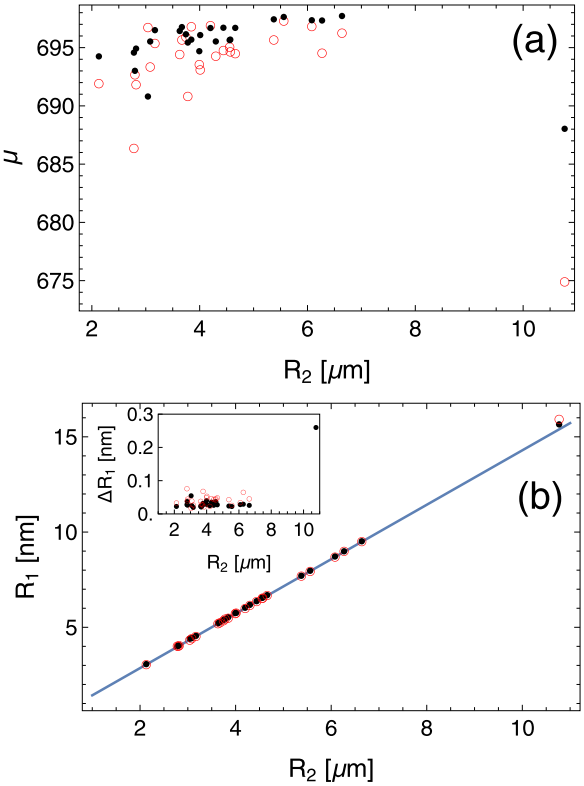

FIG. 6. (a) Radii ratio μ and (b) core radius R_1 extracted from S_0 (black dots) and τ_0 with $\Gamma = 20\ \frac{ms}{Kg}$ (red open circles). The blue line marks our result for a critical hedgehog, Eq. (49), with μ_c as stated in Eq. (45). The inset zooms in on the deviation $\Delta R_1 = R_1 - R_2/\mu_c$ of the experimental points from the critical hedgehog line. All points correspond to drops that exhibited large fluctuations.

B. The core radius

About 50% of our experimental drops showed giant fluctuations. In our discussion here, we focus on these drops as we did in our experiments.

A common feature of all drops that display giant fluctuations in our experiments is that though the mean positions of their central droplets at the core can easily be determined, their size is too small to be measured optically in our microscope; this observation suggests that these droplets are likely to be smaller than 0.1 μm in radius. This precludes a direct measurement of R_1. However, we can utilize the theoretical predictions derived above to extract R_1 from our experimental data shown in Fig. 5. We have two unknowns, κ and μ (Γ will be discussed below), and we need two equations to evaluate them. Equation (48) provides an analytic expression relating κ^2 to μ, leaving us with one unknown, which we calculate by setting the measured values of S_0 plotted in Fig. 5 equal to the formula for $S_0(r_{\rm probe}, t = 0)$ [Eq. (48)] as a function of κ and μ but with κ replaced by $\kappa(\mu)$. This gives us a nonlinear function that Mathematica can easily solve for μ for each value of R_2. The results are shown in Fig. 6(a). Once we have calculated μ we obtain R_1 through the relation $R_1 = R_2/\mu$ as shown in Fig. 6(b).

We can in principle also determine μ from τ_0, whose algebraic expression in Eq. (5) is simpler than that of S_0. There is a problem, however, because τ_0 depends on the unknown quantity Γ. We have two options: (i) We can use Γ as a fit parameter. In this case, it turns out that the resulting curve $R_1(R_2)$ is remarkably insensitive to the value Γ; any value larger than roughly 10 $\frac{\rm ms}{\rm Kg}$ leads to essentially the same outcome. (ii) We can combine $S_0(r_{\rm probe}, 0)$ and τ_0 and extract Γ for each R_2 from the combined data. In this case, we find a large scatter, $\Gamma = 28.9 \pm 9.6\ \frac{\rm ms}{\rm Kg}$; see Fig 7. However, the scatter is not large enough to alter $R_1(R_2)$. Ultimately, both the data sets for $S_0(0)$ and τ_0 lead to highly consistent estimates for R_1 as a function of R_2; see Fig. 6.

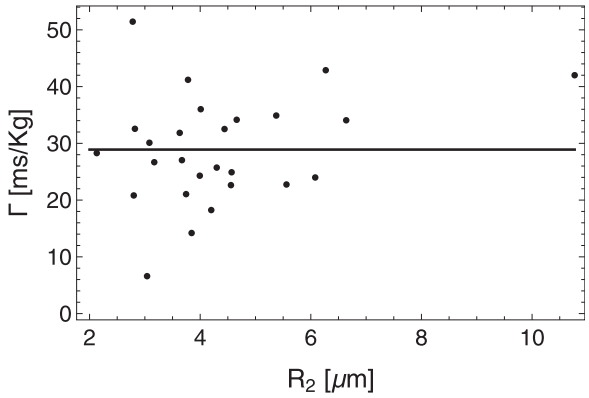

FIG. 7. Γ obtained from the combined data for S_0 and τ_0. The horizontal line represents the mean value, $\Gamma = 28.9\ \frac{\rm ms}{\rm Kg}$.

A striking feature of the plots in Fig. 6 is that only one black point in Fig. 6(a) differs from $\mu_c \approx 700$ by more than one percent (but only marginally so). The result is that R_1 in Fig. 6(b) differs from the straight line $R_1 = R_2/\mu_c$ by less than one percent. This behavior is a direct consequence of our restricting measurements to drops with fluctuations large enough to be visible, a situation that only occurs in drops near the critical point. Our analysis suggests that R_1 varies from 5 to 25 nm, albeit with most cores between 5 and 12 nm. These numbers are comparable to those found in experiments on defect cores [6,34,35] and are consistent with recent experimental insights about the nanostructure of topological defects [18] and theoretical work on the structure of nematic hedgehogs [20,36,37].

As mentioned above, essentially any value of Γ larger than 10 $\frac{\rm ms}{\rm Kg}$ leads to results for $R_1(R_2)$ based on our data for τ_0 that are highly consistent with the results based on our data for S_0. This finding is compatible with the established values of Γ for 5CB which lie in the 10 to 20 $\frac{\rm ms}{\rm Kg}$ range at room temperature, cf. Sec. III. The mean value of Γ shown in Fig. 7 lies somewhat above this range.

The large scatter in the data for Γ (as well as systematic shifts) could arise from fluctuations in average sample temperature or inhomogeneous local temperature fluctuations due to light focusing. See the experimental paper for details.

V. A ONE-DIMENSIONAL MODEL

The Frank free energy in spherical coordinates has a special feature. The operators $D_m^{\chi\chi'}$ in Eq. (7) all consist of a homogeneous term multiplied on the left by $1/r^2$, a factor that can be canceled by the r^2 factor in the volume measure

$d^3r = r^2 dr dx d\phi$. This means that as long as no other terms without the $1/r^2$ factor are introduced, the energy becomes equivalent to a kind of effective 1D theory with measure dr after integrating over $\sin\theta d\theta d\phi$. It is this fact that establishes an equivalence between our calculations and those of RS for the critical point but not for eigenvalues other than the zero one.

Here we focus only on the $m = 0$ reduced, effective 1D theory constructed from the harmonic energy of Eqs. (5) and (7a) expressed in terms of $f_0 = f_{m=0}$ only:

$$F_0 = \pi K_3 \int_{R_1}^{R_2} dr dx\, f_0 \left(D^r + \beta_2 D_1^x - 2\beta_1\right) f_0, \tag{66}$$

where D^r and D_1^x are defined in Eq. (8). Setting f_0 equal to a radial part $u_0(r)$ times the $l = 0$ eigenfunction $\sqrt{1-x^2}/\sqrt{2}$ of D_1^x: $f_0 = u_0\sqrt{1-x^2}/\sqrt{2}$, we find

$$F_0 = \pi K_3 \int_{R_1}^{R_2} dr\, u_0 \left(D^r + 2\beta_2 - 2\beta_1\right) u_0. \tag{67}$$

This is now a 1D theory in r, for which we can set $\delta u_0(r)/\delta u_0(r') = \delta(r - r')$ to obtain

$$\frac{\delta F_0}{\delta u_0(r)} = 2\pi K_3 (D^r + 2\beta_2 - 2\beta_1) u_0 = \bar{\varepsilon} u_0, \tag{68}$$

where $\bar{\varepsilon}$ is the excitation energy per unit length (not per unit volume) of the effective 1D theory. Setting $u_0 = L(r)/\sqrt{r}$, and applying the boundary conditions that $L(R_1) = L(R_2) = 0$, we find

$$L(r) = C_n \sin\left[n\pi \frac{\ln(r/R_1)}{\ln\mu}\right], \tag{69}$$

and

$$\bar{\varepsilon}_n = K_3\left[\frac{1}{4} + \left(\frac{n\pi}{\ln\mu}\right)^2\right] + 2K_2 - 2K_1, \tag{70a}$$

$$\bar{\varepsilon}_1 = K_3\left[\left(\nu_{00}^f\right)^2 + \left(\frac{\pi}{\ln\mu}\right)^2\right]. \tag{70b}$$

We have a hierarchy of states indexed by n. All the energy densities $\bar{\varepsilon}_n$ must be positive for stability, even though they do not correspond to measurable quantities. The critical mode in this representation is $\bar{\varepsilon}_1$. It passes through zero on exactly the same manifold calculated in RS and expressed in Eq. (46). Now, however, the RS state occurs when the energy $\bar{\varepsilon}$ passes from positive to negative (Fig. 8) as the Frank constants and/or μ are varied. Equation (46) is equivalent to the RS result and demonstrates that our calculation of the lowest energy excitation agrees with RS. In addition, our wave function for the lowest energy state at the critical point is also identical to that of RS, Eq. (69) with $n = 1$. To see this, we need to take the $k \to 0$ limit of Eq. (24). Near $s = 0$,

$$J_\nu(s) \sim \frac{1}{\Gamma(\nu+1)}\left(\frac{s}{2}\right)^\nu,$$
$$Y_\nu(s) = \frac{J_\nu(s)\cos\pi\nu - J_{-\nu}(s)}{\sin\pi\nu}, \tag{71}$$

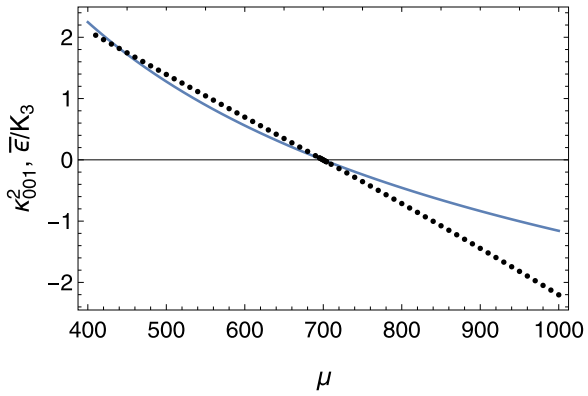

FIG. 8. Plots of $\bar{\varepsilon}/K_3$ (blue continuous line) and κ_{001}^2 (black dots), showing their common zero value at μ_c and their different shape away from μ_c.

so that

$$Z_\nu(kr) \sim \frac{1}{\sin\pi\,\nu\Gamma(1+\nu)\Gamma(1-\nu)} \times \left[-\left(\frac{kr}{2}\right)^{-\nu}\left(\frac{kR_1}{2}\right)^{\nu} + \left(\frac{kr}{2}\right)^{\nu}\left(\frac{kR_1}{2}\right)^{-\nu}\right]$$
$$\to \frac{1}{\pi\nu}\left(e^{\nu\ln(r/R_1)} - e^{-\nu\ln(r/R_1)}\right)$$
$$= \frac{2}{\pi}\sin\left(\overline{\nu}\ln r/R_1\right), \tag{72}$$

where we used $\Gamma(1-\nu)\Gamma(1+\nu) = \pi\nu/\sin\pi\nu$, $\nu = i\overline{\nu}$, and $\overline{\nu} = \pi/\ln\mu$ in the limit $k \to 0$ to reproduce Eq. (69). Thus, as expected, the two calculations of the critical point give identical results. Since the units of the two are different, the two cannot be directly compared. We can, however, compare κ_{001}^2 with $\bar{\varepsilon}/K_3$, both of which are unitless, which is done in Fig. 8.

From this discussion, it is clear that there are two distinct calculational approaches: the effective 1D approach or the full 3D approach discussed in Secs. II and III. Their predictions overlap and agree only in cases in which the functional derivatives of the energy are equal to zero. This occurs in two related cases: (1) at boundaries at which the energy of a particular harmonic mode vanishes and, perhaps more interestingly and (2) in ground states where the first functional derivatives of the Frank energy are set equal to zero. Both approaches give the same result for these calculations and, thus, the same results for the region of stability of the radial and twisted structures, but not for excitation energies, i.e., they yield different but always positive excitation energies in stable regions of the phase diagram. The 3D approach provides the energies, decay times, and correlations functions measured in real scattering experiments. It is not clear how the energies predicted by the 1D theory could be measured.

VI. CONCLUDING REMARKS

We have presented a theoretical analysis of the properties of a radial hedgehog defect in a nematic drop that complements our experimental study as reported in Ref. [22]. This analysis extends the existing treatment by RS [13]. We cal-

culate the physically measurable excitation energies of the trapped defect and the temporal correlation functions of the related director fluctuations. Most importantly, our calculations yield a critical soft mode whose energy density $\varepsilon_{001} = K_3(\kappa_{001}/R_2)^2$, where κ_{001} is analogous to a dimensionless wavenumber, vanishes at a critical value μ_c of $\mu = R_2/R_1$ that is identical to that calculated by RS [5,13] and calculated as a bound in the $\mu \to \infty$ limit in Ref. [31]. When extended to values of $\mu > \mu_c$, our calculations produce an imaginary value for κ_{001} and a resultant negative value for ε_{001} that signals that the radial state is not stable and that a transition to a lower-energy state should ensue.

The formalism (i.e., calculational procedure) we use yields energies and eigenfunctions that are measured in scattering experiments. We have not found any examples in the literature using this formalism to calculate excitation energies, etc., about captured point defects either in 3D (hedgehogs) or in 2D (strength +1 disclinations trapped in islands in freestanding smectic-*C* films). An alternative formalism has been used by RS [13] and in several papers on disclinations in 2D islands [25,26,30]. It defines the same stability limit of the radial hedgehog state (or its analog in 2D) as our formalism. The equations that determine equilibrium director configurations are the same in both formalisms, so the two yield the same equilibrium state for $\mu > \mu_c$. The excitation energies and eigenfunctions produced by the two formalisms are different as discussed in Sec. V.

An obvious next step is to calculate fluctuations relative to the +1 disclinations trapped in 2D islands in smectic-*C* freestanding films. We have begun to study this problem [28], and the results we obtained thus far follow the 3D hedgehog results quite closely. A generalization of the current calculations to include the effects of fluid flow would also be interesting, as would be the treatment of more complicated trapped defects such as hyperbolic hedgehogs [21].

To close, we compare our study to that of LT [19]. Though both studies deal with hedgehog structures in spherical nematic drops, their goals and outcomes are quite different. LT's goal was to demonstrate that a transition from a radial hedgehog to a lower-symmetry hyperbolic hedgehog could occur in response to varying Frank constants. They argued that the radial phase is most likely to be preferred when the bend constant K_3 (and to a lesser extend the twist constant K_2) is large. This is the situation that occurs in the vicinity of a transition to a smectic phase at which there is substantial fluctuation enhancement of the energy of configurations with nonzero curl [38]. They verified this conjecture and the existence of a transition upon heating (to reduce both K_3 and K_2), from a radial configuration to one with hyperbolic structure near the origin and a nonsingular +1 disclination ring at further distance from the core to satisfy the radial constraint at the the droplet boundary. They also developed an analytic model that reproduced the observed texture. The existence of the hyperbolic texture near the core rules out the radial configuration imposed in our studies.

Our goal, however, was to measure director fluctuations about a radial hedgehog state. In agreement with our theoretical calculations and earlier ones by RS [5,13] that predict the existence of a soft mode with a vanishing energy and associated divergent fluctuations, the observed fluctuation amplitude is large, particularly near the defect core. Our experiments failed to show any phase transition, and they encountered no structure that corresponded to the hyperbolic state studied by LT. This should not be surprising. Our experiments were carried out on samples in which $(\nu_{00}^f)^2 < 0$ [cf. Eq. (22)], a necessary prerequisite for the existence of a soft mode. LT provides estimates of the Frank constants near the transition to the hyperbolic state [$K_1 = 0.8 \times 10^{-6}$ dynes, $K_2 = 0.8 \times 10^{-6}$dynes, and $K_3 = 1.94 \times 10^{-6}$dynes], which yields a $K_3(\nu_{00}^f)^2 = 0.145 \times 10^{-6}$ dynes, a clearly positive value that puts their system in a completely different category from ours—one without a vanishing eigenvalue and associated large director fluctuations. It would be interesting to investigate the full phase diagram in the β_1-β_2 plane at fixed K_3, with and without the imposition of radial conditions at the core.

Finally, we note that we remain largely ignorant of the details of the development of "twist-bend" order when $\mu > \mu_c$. We have begun a numerical study [39] of this issue using the standard *Q*-based Landau-de-Gennes discretized model on a cubic mesh [40], implemented by the ALGLIB package [41], the open-source version of which is available online and described in detail in Ref. [42]. Our preliminary results do show evidence of a fairly simple twist-bend state near μ_c but more complex states as μ increases beyond μ_c.

ACKNOWLEDGMENTS

This work was supported by the NSF (Grant No. DMR20-03659), the PENN MRSEC (Grant No. DMR17-20530), including its Optical Microscopy Shared Experimental Facility, and NASA (Grant No. 80NSSC19K0348).

APPENDIX A: *f*-*g* MIXING

To evaluate $\Lambda_{mll'}$, we note that D_m^{fg} and D_m^{gf} are odd in x and that $v_{p,l}$ is even (odd) for l even (odd). Because the domain of integration over x is symmetric about zero, this implies that $\Lambda_{mll'}$ is zero unless l is even and l' is odd or vice versa. This in turn means that for any $l, l' > 0$, $A_{m,2l,n}$ couples only to $B_{m,2l'+1,n}$ and that $B_{m,2l,n}$ couples only to $A_{m,2l'+1,n}$. It is helpful to reorganize the expansion Eq. (42) to reflect these properties. To this end, we collect the expansion coefficients A_{mln} and B_{mln} in the two "vectors,"

$$\Phi^f_{mln} = \begin{pmatrix} A_{m0n} \\ B_{m1n} \\ A_{m2n} \\ B_{m3n} \\ A_{m4n} \\ \vdots \end{pmatrix} \quad \text{and} \quad \Phi^g_{mln} = \begin{pmatrix} B_{m0n} \\ A_{m1n} \\ B_{m2n} \\ A_{m3n} \\ B_{m4n} \\ \vdots \end{pmatrix}, \tag{A1}$$

so that $A_{m,2l,n} = \Phi^f_{m,2l,n}$, $B_{m,2l+1,n} = \Phi^f_{m,2l+1,n}$, $B_{m,2l,n} = \Phi^g_{m,2l,n}$ and $A_{m,2l+1,n} = \Phi^g_{m,2l+1,n}$. Reality of f and g require

$\Phi^{\chi}_{-mln} = \Phi^{\chi *}_{mln}$ for $\chi = f, g$. This leads us to

$$F = \frac{1}{2}\sum_{ln}\left[A^2_{0ln}\varepsilon^f_{0ln} + B^2_{0ln}\varepsilon^g_{0ln}\right] + \sum_{m>0,ll'nn'}\left[\Phi^{f*}_{mln}K^{ff}_{mll'nn'}\Phi^f_{ml'n'} + \Phi^{g*}_{mln}K^{gg}_{mll'nn'}\Phi^g_{ml'n'}\right], \tag{A2}$$

as our final expression for the Frank energy, where, in principle, K^{ff} and K^{gg} are infinitely large matrices. In practice, we have to approximate the Frank energy by truncating these matrices. As mentioned above, we work with $0 \leqslant m \leqslant 3$, $0 \leqslant l \leqslant 2$ and $n = 1$, which leads to the truncated matrices

$$K^{ff}_m = \begin{pmatrix} \varepsilon^f_{m01} & -im\,\Theta_{m0111} & 0 \\ im\,\Theta_{m0111} & \varepsilon^g_{m11} & im\,\Theta_{m2111} \\ 0 & -im\,\Theta_{m2111} & \varepsilon^f_{m21} \end{pmatrix}, \tag{A3}$$

and

$$K^{gg}_m = \begin{pmatrix} \varepsilon^g_{m01} & im\,\Theta_{m1011} & 0 \\ -im\,\Theta_{m1011} & \varepsilon^f_{m11} & -im\,\Theta_{m1211} \\ 0 & -im\,\Theta_{m1211} & \varepsilon^g_{m21} \end{pmatrix}, \tag{A4}$$

which are sufficient to produce good agreement with our experiments. Note that these matrices are Hermitian with complex entries, implying that the wave functions and correlation functions are also complex. Here and in the following, we use for our energy matrices the shorthand notation $K^{\chi\chi}_m = (K^{\chi\chi}_{m11})_{ll'}$. Note that once we specify the values of the Frank elastic constants and the radii R_1 and R_2, the matrix elements of K^{ff}_m and K^{gg}_m are merely numbers that we can compute, e.g., using Mathematica. In the following, we will suppress the index n, which we keep fixed at $n = 1$, for notational simplicity.

The $m = 0$ case is discussed in Sec. III. Now, we turn to $m \neq 0$. As in Sec. III, we initially focus on f with the understanding that corresponding equations exist for g (simply with f replaced by g). The equations of motion for A_{0ln} (and B_{0ln}) are given in Eq. (51) and those for Φ^f_{ml} with $m > 0$ are

$$\partial_t\,\Phi^f_{lm} = -\Gamma\frac{\partial F}{\partial \Phi^{f*}_{ml}} = -\Gamma\left(K^{ff}_m\right)_{ll'}\Phi^f_{ml'}. \tag{A5}$$

To solve these equations of motion for $m > 0$, we diagonalize K^{ff}_m,

$$\left(K^{ff}_m\right)_{ll'} = \sum_\alpha r^f_{\alpha m}\,\xi^f_{\alpha ml}\xi^{f*}_{\alpha ml'}, \tag{A6}$$

where the $\xi^f_{\alpha ml}$, which are complex, are the components of the normalized eigenvectors of K^{ff}_m, and $r^f_{\alpha m}$ are the corresponding eigenvalues. Expressing Φ^f_{ml} in terms of the basis provided by these eigenvectors, we have

$$\Phi^f_{ml} = \sum_\alpha \Phi^f_{\alpha m}\,\xi^f_{\alpha ml}, \tag{A7}$$

where $\Phi^{f*}_{\alpha m} = \Phi^f_{\alpha(-m)}$ and $\xi^{f*}_{\alpha(-m)l} = \xi^f_{\alpha ml}$. Inserting Eqs. (A6) and (A7) into Eq. (A5), the equations of motion for $m > 0$ simplify to

$$\partial_t\,\Phi^f_{\alpha m} = -\Gamma\, r^f_{\alpha m}\Phi^f_{\alpha m} \tag{A8}$$

and are readily solved, yielding

$$\Phi^f_{\alpha m}(t) = \Phi^f_{\alpha m}(0)\,e^{-\Gamma\, r^f_{\alpha m}t}. \tag{A9}$$

For the Φ^f-Φ^f correlations, this leads to

$$\left\langle \Phi^{f*}_{ml}(t)\Phi^f_{ml'}(0)\right\rangle = k_BT\; G^f_{mll'}(t), \tag{A10}$$

where

$$G^f_{mll'}(t) = \sum_\alpha \frac{1}{r^f_{\alpha m}}\,\xi^f_{\alpha ml}\xi^{f*}_{\alpha ml'}\,e^{-\Gamma\, r^f_{\alpha m}t}. \tag{A11}$$

Clearly, $G^f_{(-m)ll'}(t) = G^f_{ml'l}(t) = G^{f*}_{mll'}(t)$.

From here on, it is useful to distinguish between f and g superscripts again. Recalling that $A_{2l,mn} = \Phi^f_{2l,mn}$ and $A_{2l+1,mn} = \Phi^g_{2l+1,mn}$ from the definitions of Φ^f_{lmn} and Φ^g_{lmn} in Eq. (A1), we obtain

$$\langle A^*_{m,2l}(t)A_{m,2l'}(0)\rangle = k_BT\; G^f_{m,2l,2l'}(t), \tag{A12a}$$

$$\langle A^*_{m,2l+1}(t)A_{m,2l'+1}(0)\rangle = k_BT\; G^g_{m,2l+1,2l'+1}(t). \tag{A12b}$$

Having the time-dependent correlations of the A-coefficients for $m = 0$ and $|m| > 0$, we are now in the position to write down the time-dependent f-f correlation function. Collecting terms, we obtain Eq. (55) for the f-f correlation functions with the $m = 0$ contribution given by Eq. (56) the $|m| > 0$ functions by

$$S_m(r, r', x, x', t) = S^*_{-m}(r, r', x, x', t) = \frac{k_BT}{2\pi} \times \sum_{ll'n}\left\{G^f_{m,2l,2l'}(t)w_{m,2l}(r, x)w_{m,2l'}(r', x') + G^g_{2m,l+1,2l'+1}(t)w_{m,2l+1}(r, x)w_{m,2l'+1}(r', x')\right\}, \tag{A13}$$

where $w_{m,l(r,x)} = u^f_{m,l}(r)v^f_{m,l}(x)$. Note that for $t \to 0$, our time-dependent correlation functions reduce to their static counterparts as they should. Using Eq. (63) we can calculate $\tilde{S}_m$ in terms of the C_p's:

$$\tilde{S}_0 = \tfrac{1}{4}(C_0 + C_1 + C_2 + C_3) \tag{A14a}$$

$$\tilde{S}_1 = \tfrac{1}{4}[C_0 - C_2 + i(C_1 - C_3)] \tag{A14b}$$

$$\tilde{S}_2 = \tfrac{1}{4}(C_0 - C_1 + C_2 - C_3) \tag{A14c}$$

$$\tilde{S}_3 = \tfrac{1}{4}[C_0 - C_2 - i(C_1 - C_3)]. \tag{A14d}$$

As required, $\tilde{S}_0$ and $\tilde{S}_2$ are real, and $\tilde{S}_1$ and $\tilde{S}_3$ are complex with $\tilde{S}_3 = \tilde{S}^*_1$. In addition, $\tilde{S}_1 + \tilde{S}_3 = (C_0 + C_1)/2$ is real, and $\tilde{S}_1 - \tilde{S}_3 = (C_1 - C_3)/2i$ is pure imaginary.

APPENDIX B: LIGHT TRANSMISSION

We find it worthwhile to elaborate some more on the connection of above results to various quantities directly measurable by spectroscopy experiments. First, let us discuss

the connection to the polarized microscope images taken in our experiments [22]. We can produce theoretical versions of these images for a given random pattern specified by a set of random A_{mln} via the usual Jones Matrix formalism using

$$\delta\mathbf{n}(\vec{r},t) = \hat{e}_\phi \sum_{mln} A_{mln}(t)\Psi^f_{mln}(\vec{r}). \tag{B1}$$

To facilitate this, we simply have to draw the A_{mln} from their Gaussian distribution whose variance is given by Eqs. (53) and (A12). Figure 5 of Ref. [22] shows measured and theoretical polarized microscope images that are in close agreement.

Next, we turn to the dielectric tensor and refractive index of our nematic drop. As is customary for a nematic, we approximate the dielectric tensor by writing

$$\begin{aligned}\varepsilon_{ij}(\vec{r},t) =& \varepsilon_\parallel n_i(\vec{r},t)n_j(\vec{r},t) \\ &+ \varepsilon_\perp[\delta_{ij} - n_i(\vec{r},t)n_j(\vec{r},t)],\end{aligned} \tag{B2}$$

where $\varepsilon_\parallel$ and $\varepsilon_\perp$ are the components parallel and perpendicular to the director, respectively. The corresponding refractive index $\nu_{ij} = \sqrt{\varepsilon_{ij}}$ is

$$\begin{aligned}\nu_{ij}(\vec{r},t) =& \sqrt{\varepsilon_\parallel}\, n_i(\vec{r},t)n_j(\vec{r},t) \\ &+ \sqrt{\varepsilon_\perp}[\delta_{ij} - n_i(\vec{r},t)n_j(\vec{r},t)].\end{aligned} \tag{B3}$$

To first order in the deviation $\delta\mathbf{n}(\vec{r},t)$ from the radial equilibrium configuration $\mathbf{n}^0(\vec{r}) = \hat{e}_r$, the fluctuations $\delta\varepsilon_{ij}$ and $\delta\nu_{ij}$ of these quantities are

$$\delta\varepsilon_{ij}(\vec{r},t) = \Delta\varepsilon\big[n^0_i(\vec{r})\delta n_j(\vec{r},t) + n^0_j(\vec{r})\delta n_i(\vec{r},t)\big], \tag{B4}$$

where $\Delta\varepsilon = \varepsilon_\parallel - \varepsilon_\perp$ is the dielectric anisotropy, and

$$\delta\nu_{ij}(\vec{r},t) = \Delta\nu\big[n^0_i(\vec{r})\delta n_j(\vec{r},t) + n^0_j(\vec{r})\delta n_i(\vec{r},t)\big], \tag{B5}$$

where $\Delta\nu = \sqrt{\varepsilon_\parallel} - \sqrt{\varepsilon_\perp}$. If desired, one can now readily calculate random samples of $\delta\varepsilon_{ij}$ and $\delta\nu_{ij}$ using Eq. (B1).

Beyond that, we can also calculate the fluctuations of the dielectric constant, the scattered electrical field, the light intensity profile, etc. Denoting the electric polarization directions of the incident and transmitted light by $\hat{e}^I$ and $\hat{e}^T$, respectively, the magnitude of the scattered electric field is proportional to

$$E(\vec{r},t) = e^I_i\varepsilon_{ij}(\vec{r},t)e^T_j = \Delta\varepsilon\,\mathcal{N}(\vec{r})\,f(\vec{r},t), \tag{B6}$$

where

$$\mathcal{N}(\vec{r}) = e^I_r(\vec{r})e^T_\phi(\vec{r}) + e^T_r(\vec{r})e^I_\phi(\vec{r}), \tag{B7}$$

is a geometric factor containing the projections of the polarization vectors $\hat{e}^I$ and $\hat{e}^T$ onto $\hat{e}_r$ and $\hat{e}_\phi$, $e^I_r = \hat{e}^I\cdot\hat{e}_r$, etc. The correlation function of the electric field magnitude follows as

$$\langle E(\vec{r},t)E(\vec{r}',0)\rangle = (\Delta\varepsilon)^2\mathcal{N}(\vec{r})\mathcal{N}(\vec{r}')\langle f(\vec{r},t)f(\vec{r}',0)\rangle, \tag{B8}$$

or, collecting from our results above,

$$\begin{aligned}\langle E(\vec{r},t)E(\vec{r}',0)\rangle =& (\Delta\varepsilon)^2\mathcal{N}(\vec{r})\mathcal{N}(\vec{r}') \\ &\times\sum_{m=0}^{\infty} S_m(r,r',x,x',t)\cos[m(\phi-\phi')].\end{aligned} \tag{B9}$$

From this, the average intensity of the transmitted light is readily obtained using

$$\langle I(\vec{r})\rangle = \langle E^2(\vec{r},0)\rangle. \tag{B10}$$

Another quantity of potential interest is the intensity correlation function

$$\langle I(\vec{r},t)I(\vec{r}',0)\rangle = \langle E^2(\vec{r},t)E^2(\vec{r}',0)\rangle. \tag{B11}$$

Exploiting the common properties of Gaussian distributions, we get

$$\begin{aligned}\langle I(\vec{r},t)I(\vec{r}',0)\rangle =& (\Delta\varepsilon)^4\mathcal{N}^2(\vec{r})\mathcal{N}^2(\vec{r}')[\langle f^2(\vec{r},t)\rangle\langle f^2(\vec{r}',0)\rangle \\ &+ 2\langle f(\vec{r},t)f(\vec{r}',0)\rangle^2],\end{aligned} \tag{B12}$$

with the correlations of f as given in Eq. (55).

[1] P.-G. de Gennes and J. Prost, *The Physics of Liquid Crystals*, 2nd ed. (Oxford Science Publications, Oxford, UK, 1993).
[2] P. M. Chaikin and T. C. Lubensky, *Principles of Condensed Matter Physics* (Cambridge University Press, Cambridge, UK, 1995).
[3] P. J. Collings and J. W. Goodby, *Introduction to Liquid Crystals: Chemistry and Physics*, 2nd ed. (CRC Press, Boca Raton, FL, 2019).
[4] S. Chandrasekhar and Ranganath, Adv. Phys. **35**, 507 (1986).
[5] H. Stark, Phys. Rep. **351**, 387 (2001).
[6] R. Repnik, L. Mathelitsch, M. Svetec, and S. Kralj, Eur. J. Phys. **24**, 481 (2003).
[7] M. Kleman and O. D. Lavrentovich, Philos. Mag. **86**, 4117 (2006).
[8] G. P. Alexander, Bryan Gin-ge Chen, E. A. Matsumoto, and R. D. Kamien, Rev. Mod. Phys. **84**, 497 (2012).
[9] M. J. Press and A. S. Arrott, Phys. Rev. Lett. **33**, 403 (1974).
[10] M. J. Press and A. S. Arrott, J. Phys. Colloques **36**, C1-177 (1975).
[11] P. Poulin, H. Stark, T. C. Lubensky, and D. A. Weitz, Science **275**, 1770 (1997).
[12] P. Poulin and D. A. Weitz, Phys. Rev. E **57**, 626 (1998).
[13] A. Rüdiger and H. Stark, Liq. Cryst. **26**, 753 (1999).
[14] A. Sonnet, A. Kilian, and S. Hess, Phys. Rev. E **52**, 718 (1995).
[15] C. Chiccoli, P. Pasini, F. Semeria, T. J. Sluckin, and C. Zannoni, J. Phys. II **5**, 427 (1995).
[16] E. C. Gartland and S. Mkaddem, Phys. Rev. E **59**, 563 (1999).
[17] S. Mkaddem and E. C. Gartland, Phys. Rev. E **62**, 6694 (2000).
[18] X. G. Wang, Y. K. Kim, E. Bukusoglu, B. Zhang, D. S. Miller, and N. L. Abbott, Phys. Rev. Lett. **116**, 147801 (2016).
[19] O. D. Lavrentovich and E. M. Terentjev, Sov. Phys. JETP **64**, 1237 (1986).
[20] S. Kralj and E. G. Virga, J. Phys. A: Math. Gen. **34**, 829 (2001).
[21] R. James and J. I. Fukuda, Phys. Rev. E **89**, 042501 (2014).

[22] A. de la Cotte, O. Stenull, S. Ettinger, P. J. Collings, T. C. Lubensky, and A. G. Yodh, Phys. Rev. E **105**, 044702 (2022).
[23] It is common practice to refer to the state signaled by the instability of the radial state as a twisted state. We prefer twist-bend state because the existence of spatially varying twist necessarily implies bend as well.
[24] C. S. Rosenblatt, R. Pindak, N. A. Clark, and R. B. Meyer, Phys. Rev. Lett. **42**, 1220 (1979).
[25] K.-K. Loh, I. Kraus, and R. B. Meyer, Phys. Rev. E **62**, 5115 (2000).
[26] P. V. Dolganov and P. Cluzeau, Phys. Rev. E **90**, 062501 (2014).
[27] K. Harth and R. Stannarius, Front. Phys. **8**, 00112 (2020).
[28] O. Stenull and T. C. Lubensky, Crystals **12**, 1 (2022).
[29] A. Eremin, C. Bohley, and R. Stannarius, Euro. Phys. J. E **21**, 57 (2006).
[30] J. B. Lee, D. Konovalov, and R. B. Meyer, Phys. Rev. E **73**, 051705 (2006).
[31] R. Cohen and M. Taylor, Commun. Partial Diff. Eq. **15**, 675 (1990).
[32] S. T. Wu and C. S. Wu, Phys. Rev. A **42**, 2219 (1990).
[33] A. V. Zakharov, A. V. Komolkin, and A. Maliniak, Phys. Rev. E **59**, 6802 (1999).
[34] D. Svenšek and S. Žumer, Phys. Rev. E **66**, 021712 (2002).
[35] N. Schopohl and T. J. Sluckin, J. Phys. (France) **49**, 1097 (1988).
[36] C. Chiccoli, P. Pasini, F. Semeria, T. J. Sluckin, and C. Zannoni, J. Phys. II (France) **5**, 427 (1995).
[37] F. Greco and G. Marruci, Mol. Cryst. Liq. Cryst. Sci. Technol., Sect. A **210**, 129 (1992).
[38] F. Jahnig and F. Brochard, J. Phys. France **35**, 301 (1974).
[39] S. Ettinger, O. Stenull, P. J. Collings, A. de la Cotte, T. C. Lubensky, and A. J. Yodh (unpublished).
[40] M. Ravnik and S. Žumer, Liq. Cryst. **36**, 1201 (2009).
[41] Alglib, www.alglib.net.
[42] D. M. Sussman and D. A. Beller, Front. Phys. **7**, 204 (2019).